

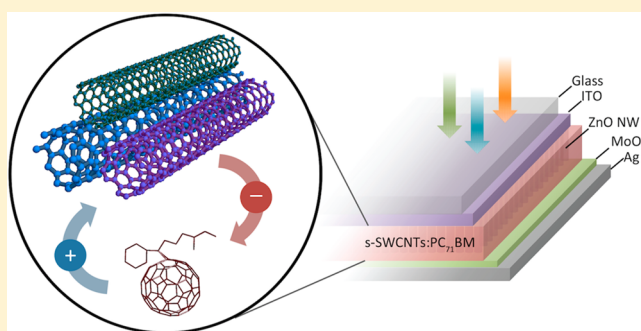
## Polychiral Semiconducting Carbon Nanotube–Fullerene Solar Cells

Maogang Gong,<sup>†,⊥</sup> Tejas A. Shastry,<sup>‡,⊥</sup> Yu Xie,<sup>†</sup> Marco Bernardi,<sup>||</sup> Daniel Jason,<sup>†</sup> Kyle A. Luck,<sup>‡</sup> Tobin J. Marks,<sup>‡,§</sup> Jeffrey C. Grossman,<sup>||</sup> Shenqiang Ren,<sup>\*,†</sup> and Mark C. Hersam<sup>\*,‡,§</sup><sup>†</sup>Department of Chemistry, University of Kansas, Lawrence, Kansas 66045, United States<sup>‡</sup>Department of Materials Science and Engineering, Northwestern University, Evanston, Illinois 60208, United States<sup>§</sup>Department of Chemistry, Northwestern University, Evanston, Illinois 60208, United States<sup>||</sup>Department of Materials Science and Engineering, Massachusetts Institute of Technology, Cambridge, Massachusetts 02139, United States

## Supporting Information

**ABSTRACT:** Single-walled carbon nanotubes (SWCNTs) have highly desirable attributes for solution-processable thin-film photovoltaics (TFPVs), such as broadband absorption, high carrier mobility, and environmental stability. However, previous TFPVs incorporating photoactive SWCNTs have utilized architectures that have limited current, voltage, and ultimately power conversion efficiency (PCE). Here, we report a solar cell geometry that maximizes photocurrent using polychiral SWCNTs while retaining high photovoltage, leading to record-high efficiency SWCNT–fullerene solar cells with average NREL certified and champion PCEs of 2.5% and 3.1%, respectively. Moreover, these cells show significant absorption in the near-infrared portion of the solar spectrum that is currently inaccessible by many leading TFPV technologies.

**KEYWORDS:** carbon nanomaterials, photovoltaic, bulk heterojunction, nanowires



Thin-film photovoltaic (TFPV) technologies focus on producing efficient solar cells with materials amenable to low-cost processing techniques.<sup>1,2</sup> Recently, we and other groups have proposed and implemented solar cells based on carbon nanomaterials<sup>3–9</sup> as an avenue toward solution-processable photovoltaics that utilize components with broad spectral absorption and high carrier mobility, as well as thermal, chemical, and optical stability.<sup>10–13</sup> In particular, single-walled carbon nanotubes (SWCNTs) are well-known to strongly absorb visible and near-infrared (NIR) light in contrast to typical conjugated organic polymers that are limited to the ultraviolet/visible range. Moreover, the exciton lifetime, carrier mobility, and photostability of carbon nanomaterials rival or exceed those of typical donor polymers and many other TFPV materials.<sup>10,14–17</sup> Increasingly large-scale production of high purity SWCNTs offers promise for a low-cost, high-performance photovoltaic material,<sup>18</sup> but several factors have limited significant performance advances for SWCNT–fullerene solar cells.

SWCNTs are generally synthesized in mixed purity (1/3 metallic, 2/3 semiconducting), thus presenting variability in electronic structure that necessitates postsynthesis sorting.<sup>19,20</sup> Blends of small-diameter semiconducting SWCNTs (*s*-SWCNTs) with diameter  $d < 1.2$  nm and the fullerene derivative (6,6)-phenyl- $C_{71}$ -butyric acid methyl ester (PC<sub>71</sub>BM) can form type-II heterojunctions capable of exciton dissociation and photovoltaic operation, in which *s*-SWCNTs behave as the

electron donor and PC<sub>71</sub>BM as the electron acceptor material.<sup>3</sup> Such small-diameter SWCNTs have previously shown significant aggregation and the formation of coarse morphologies inadequate for efficient bulk-heterojunction (BHJ) solar cells.<sup>3</sup> Furthermore, devices based on *s*-SWCNT–fullerene bilayers have produced low efficiencies due to the small interfacial area between the two components.<sup>4–6</sup> The range of available *s*-SWCNT chiralities further presents a design and control challenge in that each chirality preferentially absorbs a different portion of the solar spectrum and forms a distinct heterojunction with the fullerene component.<sup>21</sup> Consequently, many researchers have employed a narrow range of SWCNT chiralities to reduce design and control complexity, although this choice may ultimately limit overall power conversion efficiency (PCE).

Our solution-processed BHJ TFPVs are based on active layers consisting of polychiral semiconducting SWCNTs and the PC<sub>71</sub>BM fullerene that are interfaced with carrier-selective contacts. This solar cell design concurrently addresses many issues that have limited previous SWCNT TFPVs, thus avoiding traditional performance trade-offs. The polychiral nature of the *s*-SWCNT distribution and smaller optical gap of the PC<sub>71</sub>BM fullerene lead to broadband optical absorption

Received: June 23, 2014

Published: August 7, 2014

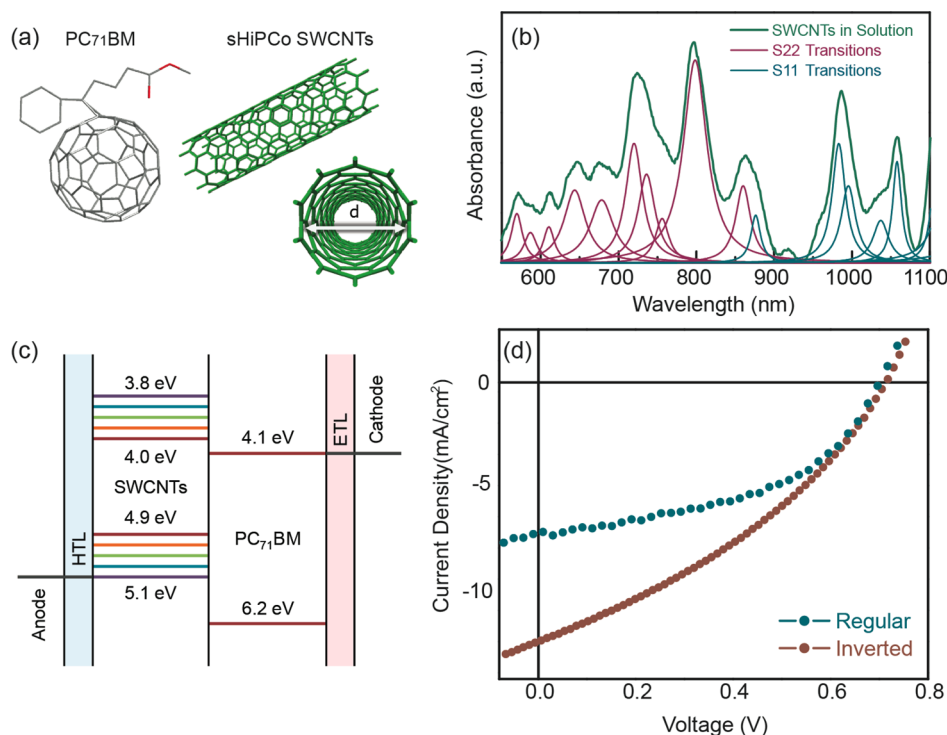


**Figure 1.** Materials, device structure, and performance of SWCNT–fullerene solar cells. (a) Structure of the carbon nanomaterials employed in this work, where the diameter of the semiconducting SWCNTs is in the 0.8–1.2 nm range. (b) Optical absorption spectra of the semiconducting SWCNTs in solution, where the  $S_{11}$  and  $S_{22}$  semiconducting transitions have been fit to Lorentzian lineshapes. Identification of the chiralities is available in Table S1, Supporting Information. (c) Schematic structure of a SWCNT/PC<sub>71</sub>BM solar cell with a proposed energy diagram for the polychiral SWCNTs with various band gaps forming type-II heterojunctions with PC<sub>71</sub>BM. (d) Current–voltage curves in the dark and under AM 1.5 illumination for a regular and an inverted geometry SWCNT/PC<sub>71</sub>BM solar cell providing a PCE of 2.5% and 3.1%, respectively.

throughout the visible and NIR regions to increase photocurrent and reduce the processing required to isolate a narrow single-chirality distribution of SWCNTs. In parallel, increasing the work function of the hole transport layer (HTL) affords simultaneous photovoltage enhancement. Furthermore, proper selection of materials processing parameters ensures a SWCNT–fullerene BHJ morphology that is favorable for charge separation. Overall, our approach overcomes key obstacles that have impeded the utilization of SWCNTs in TFV active layers, enabling a near-doubling of the current record PCE up to 3.1%.

The carbon nanomaterials used in this work are shown in Figure 1a and include the PC<sub>71</sub>BM fullerene and polychiral *s*-SWCNTs with diameters predominantly in the 0.8–1.2 nm range.<sup>19</sup> Solutions of the resulting polychiral *s*-SWCNTs show broad spectral absorption throughout the visible and NIR regions (Figure 1b) from the first ( $S_{11}$ ) and second ( $S_{22}$ ) order *s*-SWCNT optical transitions of the 21 SWCNT chiralities characterized in Table S1, Supporting Information.<sup>22,23</sup> To disperse the *s*-SWCNTs in the blend solution and lessen micron-scale bundling, a small amount (~1 wt %) of hole-conducting polymer, poly[(9,9-dioctylfluorenyl-2,7-diyl)-*co*-(4,4'-(*N*-(4-*s*-butylphenyl))-diphenylamine)] (TFB) or poly-(3-hexylthiophene-2,5-diyl) (P3HT), is used for regular and inverted geometry cells, respectively.<sup>24</sup> A diameter of ~2 nm is observed for the polymer-functionalized SWCNTs under transmission electron microscopy (TEM) (Figure S1a, Supporting Information). Atomic force microscopy indicates that large, micron-scale SWCNT bundles and/or PC<sub>71</sub>BM aggregates are nearly absent in BHJ active layers deposited using optimized conditions (Figure S1b, Supporting Informa-

tion). This characterization suggests that the SWCNTs are well dispersed into at most few-SWCNT bundles by the polymer, and the hybrids are well distributed within the PC<sub>71</sub>BM matrix. This morphology maximizes the interfacial area between SWCNT and PC<sub>71</sub>BM domains, thus facilitating efficient exciton dissociation and charge separation.

The configuration of the present cells consists of BHJ SWCNTs/PC<sub>71</sub>BM blends as the active layer sandwiched between electron and hole transport layers (ETL and HTL, respectively) and electrical contacts. Because of the polychiral nature of the SWCNTs, a range of SWCNT band gaps are available for absorption within the cell leading to the proposed band diagram and cell configuration in Figure 1c. All of the chiralities present form type-II heterojunctions with the PC<sub>71</sub>BM fullerene, and the smallest band gap SWCNTs (Table S1, Supporting Information) set an upper limit on the open-circuit voltage of ( $V_{oc}$ ) ~0.8 V. Figure 1d shows champion  $J$ – $V$  curves of regular and inverted geometry cells under AM 1.5 illumination with PCEs of 2.5% and 3.1%, respectively (Table S2, Supporting Information). Both of these cells exhibit PCEs higher than the most recent PCE record of 1.7% for solar cells employing SWCNTs as a photoactive component under AM 1.5 illumination.<sup>3,5–7,25</sup> From the same batch of regular geometry cells with a poly(3,4-ethylenedioxythiophene) poly(styrenesulfonate) (PEDOT:PSS)/TFB HTL and a bathocuproine (BCP) ETL, we observe an average PCE of  $2.3\% \pm 0.2\%$ , with variability primarily in the short-circuit current density and fill factor (Table S3, Supporting Information). We attribute this variability in fill factor and current to variations in the percolating network of SWCNTs with different band gaps.<sup>5</sup> Our inverted cell geometry shows

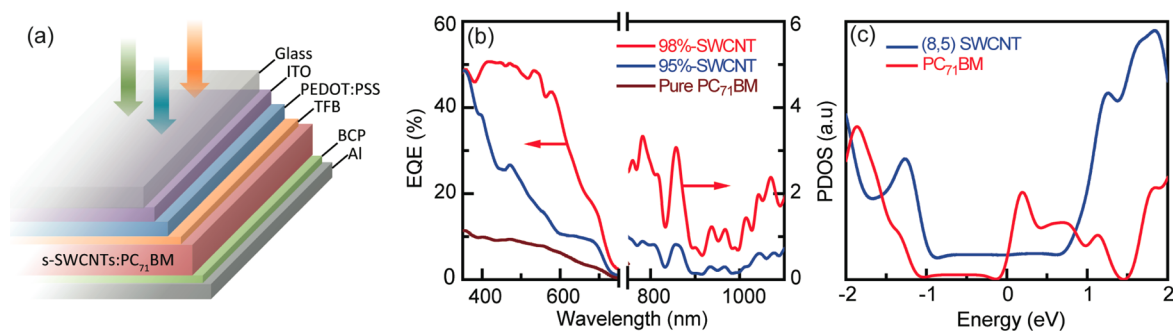


**Figure 2.** Effects of SWCNT semiconducting purity on device performance. (a) Device structure of regular geometry cells used for evaluating purity effects. (b) EQE plots of the selected cells in the visible and NIR regions. The EQE from a pure PC<sub>71</sub>BM cell shows a single peak at visible wavelengths of 350–700 nm. (c) PDOS plot of an interface between a (8,5) m-SWCNT and PC<sub>71</sub>BM computed using density functional theory. The energy is plotted with respect to the Fermi energy, where the LUMO level of PC<sub>71</sub>BM lies 0.2 eV above the Fermi energy of the m-SWCNT.

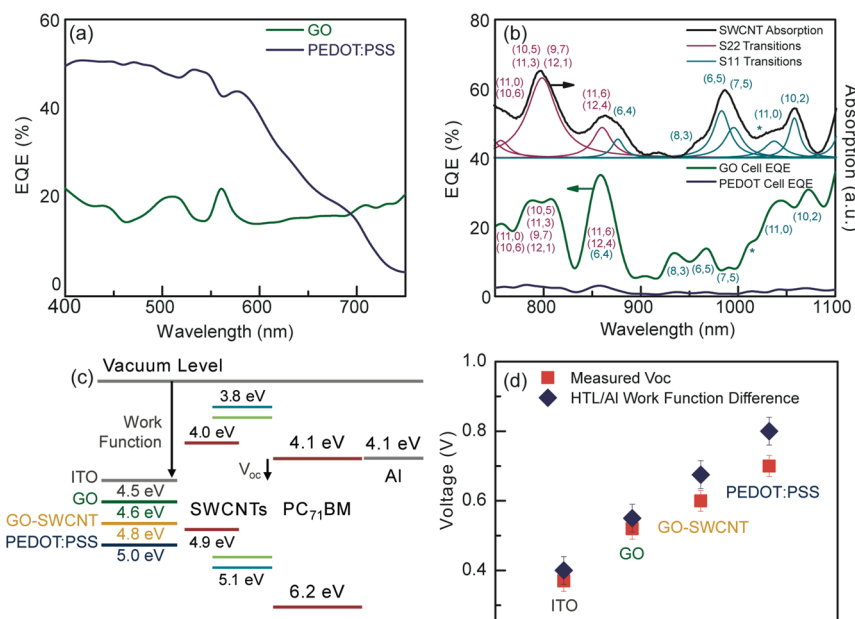


**Figure 3.** Dependence of photovoltaic performance on the HTL. (a) EQE for cells with GO and PEDOT:PSS HTLs in the visible range. (b) NIR EQE of the cells in panel a, shown together with the absorption spectrum of s-SWCNTs. The asterisk (\*) denotes phonon sidebands of the S<sub>11</sub> transition of (11,0). (c) Energy diagram showing measured work functions for ITO (no HTL), GO, GO-SWCNT, and PEDOT:PSS HTLs, the work function of the Al anode, and the HOMO and LUMO energies of representative s-SWCNTs and PC<sub>71</sub>BM. The smallest band gap (voltage limiting) SWCNT is shown in red, while the photoactive SWCNTs are shown at the junction with PC<sub>71</sub>BM. (d) Comparison of the energy difference between four different HTLs and the Al work function, and the  $V_{oc}$  measured in solar cells based on the same HTLs.

lower variability with over 100 devices (Figure S2, Supporting Information) exhibiting an average PCE of  $2.5\% \pm 0.1\%$  and a maximum PCE of 3.1% using ZnO nanowires and MoO<sub>x</sub> as the ETL and HTL, respectively. The inverted cells also show high stability in ambient conditions without encapsulation (Figure S3, Supporting Information), illustrating the exceptional chemical and environmental stability of carbon nanomaterials.

To investigate the role of the s-SWCNTs versus residual metallic SWCNT (m-SWCNT) impurities in the polychiral SWCNT samples, regular geometry solar cells were prepared using pure PC<sub>71</sub>BM (no SWCNTs), 95% semiconducting purity s-SWCNT/PC<sub>71</sub>BM, and 98% semiconducting purity s-SWCNT/PC<sub>71</sub>BM, where the principal impurities in the nanotube samples consist of metallic SWCNTs. The device structure of the cells is shown in Figure 2a, where PEDOT:PSS/TFB and BCP act as the HTL and ETL, respectively. Figure 2b shows the external quantum efficiency (EQE) of these devices, and further performance details are

found in Figure S4 and Table S4, Supporting Information. We attribute the broad EQE peak in Figure 2b between 400 and 700 nm to the photocurrent generated from light absorption in the fullerene derivative (Figure S5, Supporting Information). Features at wavelengths higher than 750 nm can be attributed to the S<sub>11</sub> and S<sub>22</sub> transitions, and the short-wavelength peaks near 540 and 590 nm correspond to S<sub>22</sub> and/or S<sub>33</sub> SWCNT transitions overlapping with the fullerene contribution. These features suggest that both fullerenes and s-SWCNTs participate in absorbing light and generating carriers. A decrease in the PCE and EQE from s-SWCNT/PC<sub>71</sub>BM cells to the pure PC<sub>71</sub>BM cell implies that s-SWCNTs play a crucial role in dissociating excitons at type-II heterojunction interfaces and efficiently transport holes to the HTL contact despite their low concentration ( $\sim 3$  wt %) in the active layer blend, which is a characteristic observed in other systems with low donor concentrations.<sup>26</sup>

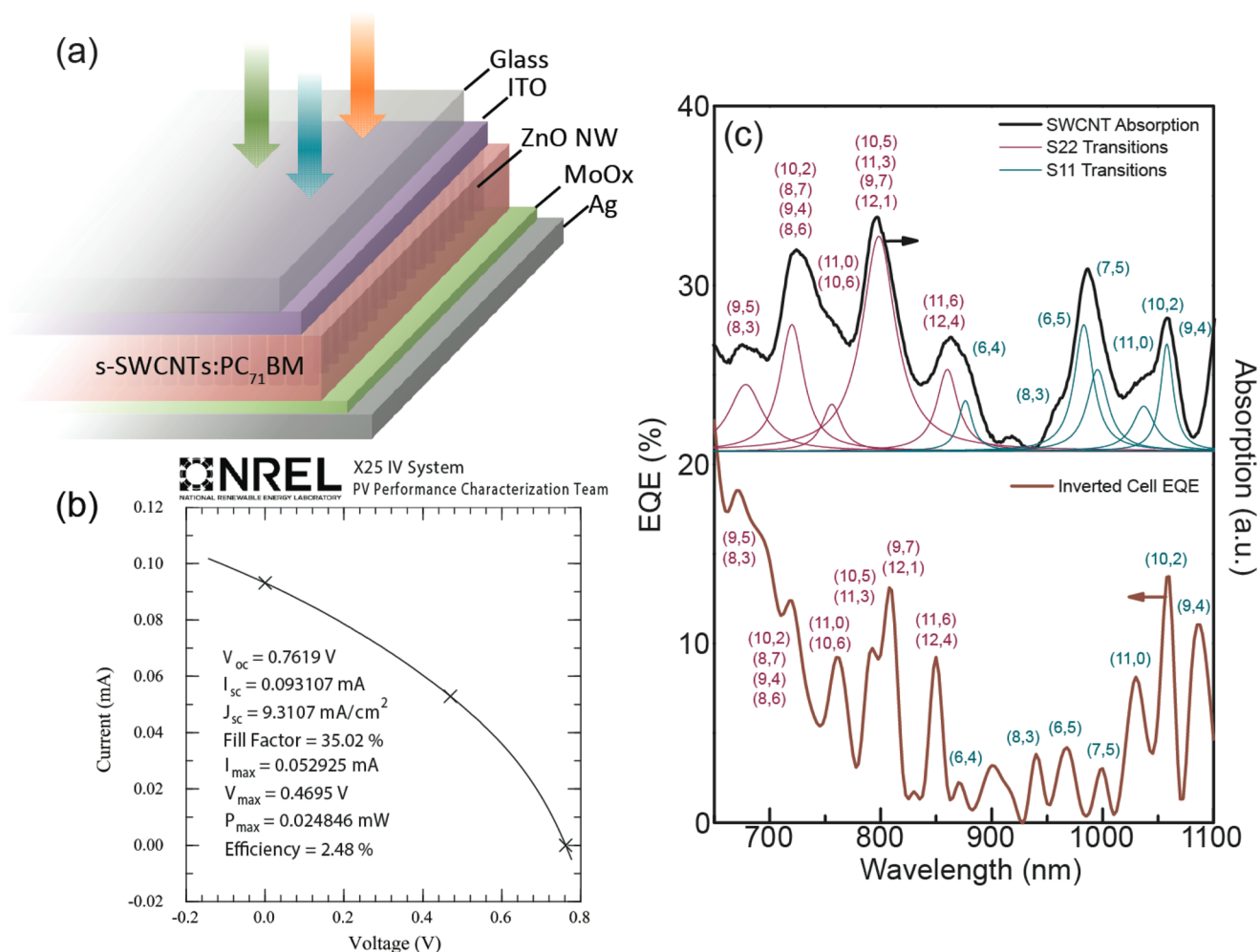


**Figure 4.** Structure and device performance of an inverted SWCNT/PC<sub>71</sub>BM solar cell. (a) Schematic structure of the inverted cell, with a ZnO nanowire ETL penetrating the active layer and a high work function MoO<sub>x</sub> HTL. (b) Current–voltage curve of an NREL certified device with a PCE of 2.5%. (c) Near-IR EQE of the inverted cell in Figure 1d plotted with the SWCNT chiral distribution, where overlap between the EQE and S<sub>11</sub>/S<sub>22</sub> absorption peaks is evident.

The PCE enhancement from 95% s-SWCNTs to 98% s-SWCNTs suggests that the metallic species primarily reduce charge collection,<sup>27</sup> as evidenced by a significant decrease in the EQE, although they do not electrically short the cells at such low concentrations. We have carried out density functional theory (DFT) calculations of an interface between PC<sub>71</sub>BM and a representative m-SWCNT with (8,5) chirality and  $d = 0.9$  nm to further investigate the adverse impact of m-SWCNTs on efficiency. Figure 2c shows the projected density of states (PDOS) of the m-SWCNT/PC<sub>71</sub>BM interface, which reveals a small ( $\sim 0.2$  eV) positive offset between the LUMO energy of PC<sub>71</sub>BM and the Fermi energy of m-SWCNTs. This alignment favors injection of electrons from PC<sub>71</sub>BM to the m-SWCNT, and thus to the SWCNT network, where they can recombine with holes transported by s-SWCNTs in the active layer. In addition, interfaces between m-SWCNTs and s-SWCNTs have been shown to form Schottky barriers with low hole transmission probabilities of  $\sim 5\%$ .<sup>28</sup> Thus, we conclude that the fraction of m-SWCNTs in the active layer must be minimized due to their adverse effects on hole transport in the s-SWCNT network.

To further characterize the absorption and photoconversion properties of the s-SWCNT/PC<sub>71</sub>BM active layers, regular geometry cells were fabricated using two different HTLs:

graphene oxide (GO) and PEDOT:PSS. As seen in Figure S6, Supporting Information, PEDOT:PSS shows strong absorption at NIR wavelengths, while GO exhibits strong absorption in the visible range. As a consequence, the cell employing PEDOT:PSS as the HTL shows a higher EQE in the visible, originating from fullerene absorption and the S<sub>22</sub>/S<sub>33</sub> s-SWCNT transitions. In the NIR EQE plotted in Figure 3b, the cell with GO as the HTL exhibits higher EQE stemming from S<sub>22</sub> and S<sub>11</sub> transitions of the s-SWCNT than the PEDOT:PSS cell. Note that because of differences between SWCNT bundling in solution compared to films, there are slight peak shifts between the absorption spectrum and EQE. Nevertheless, the highest SWCNT EQE comes from S<sub>11</sub> transitions of individual chiralities and overlapping S<sub>22</sub> transitions of several chiralities. The performance of these cells is shown in Figure S7, Supporting Information with the short-circuit current density corrected by integrating the EQE spectra against the solar spectrum for both cells. As the EQE plots do not capture the entire absorption of both cells, the corrected current values for both cells are likely to be underestimated. However, the greater visible EQE of the PEDOT:PSS cell and the greater NIR EQE of the GO cell lead to similar corrected currents in these two cases, with the PEDOT:PSS cell having a much higher open-circuit voltage.

The origin of the high  $V_{oc}$  of cells with a PEDOT:PSS HTL was explored by fabricating regular geometry cells with various HTLs including PEDOT:PSS, GO, and a blend of GO + SWCNTs. Cells fabricated with the various interfacial layers (and ITO without an HTL material) all exhibit different open-circuit voltages in Figure S8 and Table S5, Supporting Information, implying that the nature of the interfacial layer impacts the cell voltage. Figure 3c shows an energy diagram of the s-SWCNT/PC<sub>71</sub>BM blend, where the donor–acceptor interface gap ( $\Delta E_{DA}$ ) of 0.8 eV between the effective highest occupied molecular orbital (HOMO) of the smallest-gap SWCNT in our distribution and the lowest unoccupied molecular orbital (LUMO) of PC<sub>71</sub>BM sets an upper limit for  $V_{oc}$ .<sup>29</sup> We note that these small band gap SWCNTs (denoted in red in Figure 3c) may not have sufficient energetic offsets for exciton dissociation with the fullerene, but do limit voltage as they exist in a percolating network with photoactive large band gap SWCNTs (denoted in blue and green in Figure 3c). In the present cells,  $V_{oc}$  correlates with the energy difference between the work function of the HTL (Figure S9, Supporting Information) and the aluminum (Al) cathode rather than by  $\Delta E_{DA}$  as in typical organic solar cells. The comparison of  $V_{oc}$  and the HTL/Al work function difference in Figure 3d shows clear correlation between these two quantities. This  $V_{oc}$  dependence can be attributed to the absence of Fermi level pinning at the SWCNT/HTL and PC<sub>71</sub>BM/Al interfaces, implying that the metal–insulator–metal (MIM) model may apply to these carbon-based solar cells,<sup>30</sup> in contrast to the pinning in organic cells that occurs at the interface between the electrodes and the organic active layer. This assertion is further supported by Figure S10, Supporting Information, where the insensitivity of the metal work function to light intensity leads to an analogous insensitivity of  $V_{oc}$  in the range of 20 to 100 mW/cm<sup>2</sup>. Additionally, the dark  $J$ – $V$  curves of all devices prepared in this work do not show clear saturation at reverse bias due to voltage-dependent carrier injection at the Schottky barrier between the HTL and PC<sub>71</sub>BM.

To maximize light absorption throughout the visible and NIR range while maintaining a high  $V_{oc}$ , polychiral SWCNT/PC<sub>71</sub>BM cells were fabricated with the inverted device structure in Figure 4a. Zinc oxide nanowires (ZnO NWs) were used as an electron transport layer that interpenetrates the active layer to minimize the collection length within the cell and reduce morphology variability, while molybdenum oxide (MoO<sub>x</sub>) was used as a high work function HTL to maximize voltage.<sup>26</sup> This inverted cell architecture leads to record PCEs with Figure 4b containing the first published report of a carbon nanotube solar cell certified by the National Renewable Energy Lab (NREL), which independently confirms our average PCE of 2.5%.

Cross-sectional scanning electron microscopy (Figure S11, Supporting Information) verifies penetration of the active layer into a bed of ZnO NWs on ITO. Optimization of ZnO NW length and SWCNT concentration (Figure S12, Supporting Information) further contributes to the observed high performance. Additionally, a small increase in fill factor is observed on incorporation of the ZnO NWs (Figure S13, Supporting Information), indicative of improved charge extraction from the active layer. This high efficiency stems from maintaining high current resulting from both fullerenes and SWCNTs (as seen in the EQE plot in Figure 4c and Figure S14, Supporting Information) while maintaining high voltage across the cell. The high transparency of the ZnO NWs (Figure S15, Supporting Information) and the interpenetration into the

active layer provides ~70% EQE from PC<sub>71</sub>BM and over 20% of the current resulting from the  $S_{11}$  and  $S_{22}$  transitions of the polychiral s-SWCNTs in the NIR region. The inverted cell thus overcomes the trade-off in absorption based on interlayer transparency seen in the regular geometry cell and delivers stable and consistently record-high performance.

The present combination of enhanced light absorption from both PC<sub>71</sub>BM and polychiral s-SWCNTs coupled with an open-circuit voltage maximized by careful interface and electrode selection has enabled us to nearly double the efficiency of SWCNT–fullerene solar cells and represents a milestone in their development over the past decade. Our observation of high current and EQE from both the donor SWCNTs and the fullerene acceptor in a low-donor system is uncommon,<sup>26</sup> and the ability of multiple chiralities to contribute substantially to photocurrent contrasts previous work advocating single-chirality SWCNT cells.<sup>5,21</sup> The ability of these cells to absorb in the near-infrared portion of the solar spectrum opens up avenues to increase the efficiency of transparent and tandem solar cell architectures that are gaining interest in the thin-film photovoltaic community.<sup>31,32</sup> Furthermore, the utilization of sp<sup>2</sup>-bonded carbon nanomaterials implies that the present solar cell active layer has high thermal and chemical stability, thus lessening the requirements for hermetic encapsulation layers that are employed by leading TFPV technologies. By delineating the design parameters that lead to high short-circuit current, open-circuit voltage, and ultimately high PCE, this work will help guide future efforts to fully exploit carbon nanomaterials in environmentally stable photovoltaic technologies.

**Methods. SWCNT Solution Preparation.** Semiconducting single-walled carbon nanotubes (s-SWCNTs, 95% and 98% semiconducting purity) were prepared from solutions of HiPCo SWCNTs (NanoIntegris) sonicated in 1% (w/v) sodium cholate in deionized water by a 0.125 in tip horn ultrasonicator at 12 W for 60 min. Solutions were subsequently sorted by electronic type using density gradient ultracentrifugation and characterized for electronic-type purity as previously reported.<sup>19</sup> Purified fractions were combined to obtain the chiral distribution in Figure 1b. The aqueous solutions of surfactant-encapsulated s-SWCNTs were mixed with acetone to remove the surfactants and density gradient material, and the agglomerated suspensions of s-SWCNTs were subsequently vacuum filtered on a Nylon membrane. After rinsing with copious amounts of water, acetone, and isopropanol, the filtered films were dried and peeled off for use in blend solutions. Approximately 1 mg of s-SWCNTs on a 0.75 in diameter filter was necessary for the film to be thick enough to peel off successfully. The fullerene derivative (6,6)-phenyl-C<sub>71</sub>-butyric acid methyl ester (PC<sub>71</sub>BM, American Dye Source), poly[(9,9-dioctylfluorenyl-2,7-diyl)-co-(4,4'-(N-(4-s-butylphenyl))-diphenylamine)] (TFB, American Dye Source), and poly(3-hexylthiophene-2,5-diyl) (P3HT, Ossila) were used as purchased. Solutions of s-SWCNTs in 1,2-dichlorobenzene (1,2-DCB) were sonicated with TFB (regular geometry) or P3HT (inverted geometry) at a ratio of 2:1 SWCNT/polymer. The solution was then filtered to achieve functionalized s-SWCNTs, which were combined at a concentration of 2 mg/mL with PC<sub>71</sub>BM (40 mg/mL) in 1,2-DCB and stirred at 45 °C overnight.

**Chirality and Electronic Structure Determination.** An inventory of chiral species present in our samples was determined from previous photoluminescence characterization

of our sorted polychiral semiconducting HiPCo SWCNT samples (HiPCo s-SWCNT).<sup>19</sup> The absorption spectrum of HiPCo s-SWCNT was fit to Lorentzian lineshapes, and the  $S_{11}$  and  $S_{22}$  transitions of these species were matched with the fitted peaks based on a previously published empirical table.<sup>23</sup> From here, the band gap of each s-SWCNT species was also determined. The proposed band diagram shown in the main text was constructed by assuming a Fermi level of 4.5 eV for each s-SWCNT species<sup>33</sup> and calculating the effective HOMO and LUMO levels based on the  $S_{11}$  transition being symmetric about the Fermi level.<sup>34</sup> Determination of  $M_{11}$  peaks for purity evaluation was conducted based on the methods listed in our previous studies of metallic HiPCo SWCNTs.<sup>35</sup> Note that electronic-type purity determination for semiconducting HiPCo SWCNTs is restricted to ~98%, above which discrimination of the metallic  $M_{11}$  transitions that overlap with semiconducting  $S_{22}$  transitions is limited.

**ZnO Nanowire Preparation.** ZnO nanowires were grown on ITO by the hydrothermal method. ZnO seed layers were prepared by spin-coating 0.3 M zinc acetate and ethanolamine in 2-methoxyethanol solution and annealed at 180 °C for 10 min. This process was repeated twice followed by annealing in air at 400 °C for 1 h to form a uniform seed layer. The substrate was subsequently immersed into the nanowire growth solution in an autoclave for 60, 90, 120, and 210 min at 95 °C. The growth solution consisted of zinc acetate and hexamethylenetetramine at the same concentration (0.025 M) in DI water. As-grown ZnO nanowires were thoroughly rinsed with DI water and isopropanol and annealed at 300 °C for 30 min.

**General Film/Device Fabrication and Characterization.** Prepatterned indium tin oxide (ITO) glass substrates ( $0.5 \times 0.5$  in<sup>2</sup>, 20 Ohm/sq, Thin Film Devices) were cleaned by ultrasonic treatment in aqueous detergent (Alconox), deionized water, acetone, and isopropyl alcohol sequentially, followed by a UV-ozone treatment. For regular geometry cells, hole transport layers (HTLs) were fabricated via spin coating onto cleaned ITO substrates. Specifically, poly(3,4-ethylenedioxythiophene) poly(styrenesulfonate) (PEDOT:PSS, Clevis) was spin-coated on an ITO substrate to fabricate a PEDOT:PSS film. GO was prepared by a modified Hummers method. GO-SWCNT solutions were prepared by spin-coating a dispersion of purified P2-SWCNTs (Carbon Solutions, Inc.) in 1 mg/mL GO in dimethylformamide at a SWCNT loading of ~0.2 mg/mL. Samples were baked at 100 °C to remove residual water after depositing the HTLs. In a glovebox, a solution of TFB (2 mg/mL) was spin-coated on PEDOT:PSS/ITO substrates at 3000 rpm for 30 s. A solution of 3 wt % s-SWCNT and PC<sub>71</sub>BM (with 1 wt % TFB, 1,2-DCB/CHCl<sub>3</sub>, volume ratio = 0.4:0.6) was spin-coated on TFB/PEDOT:PSS/ITO substrates to make ~100 nm thick active layers. The overall solute loading for the active layer was 20 mg/mL for films spun at 800 rpm. All films were allowed to dry in covered plastic Petri dishes followed by thermal annealing at 100 °C for 10 min.

The PC<sub>71</sub>BM-only solar cells were fabricated by depositing a PC<sub>71</sub>BM solution on TFB/HTL/ITO substrates. Thermal annealing of this film was also performed at 100 °C for 10 min. BCP and Al were thermally evaporated through shadow masks at a base pressure of  $5.0 \times 10^{-6}$  Torr. For inverted cells, polyethylenimine (PEIE,  $M_w$ : 70 000 g/mol, Aldrich) was dissolved in water at a concentration of 35–40 wt % and further diluted with 2-methoxyethanol to a weight concentration of 1%. PEIE was spin-coated onto the ZnO nanowire array at 4000 rpm for 1 min. Active layer solutions were spin-

coated onto the PEIE functionalized ZnO nanowire arrays at 600 rpm for 60 s in a nitrogen-filled glovebox. The substrates were annealed at 120 °C for 10 min to ensure the infiltration of the active layer into the nanowire arrays. MoO<sub>x</sub> (5 nm, Aldrich 99.99% trace metals basis) and 100 nm Ag were thermally evaporated through shadow masks at a base pressure of  $5.0 \times 10^{-6}$  Torr at rates of 0.1 and 1 Å/s, respectively. Cells were masked using a laser-cut metal mask aligned on the devices and black electrical tape to cover reflective regions of the mask and areas of mask–device mismatch. The device areas defined by the overlap between the top and bottom electrodes and the mask were 0.6 to 1.2 mm<sup>2</sup>. Current density–voltage ( $J$ – $V$ ) plots were taken by a Keithley source generator under illumination from a calibrated solar simulator (xenon lamp, Newport) with an intensity of 100 mW/cm<sup>2</sup> and an AM 1.5 filter, and current values were corrected based on spectral mismatch between the spectrum of the xenon lamp and the solar spectrum. External quantum efficiency (EQE) measurements were carried out by a Newport system with an Oriol monochromator. The aging measurement for the unencapsulated inverted cell was carried out under ambient conditions.

**Morphology and Spectroscopic Characterization.** The inverted device cross-section and active layer were characterized using a Leo 1550 field emission scanning electron microscope (SEM) and FEI Tecnai F20 XT field emission transmission electron microscope (TEM). AFM images were taken with a Digital Instruments LFM-2 AFM/SPM microscope using silicon probes (nanoScience Instruments, Vista Probes, CLR-25, reflex coating aluminum). Absorption and transmission spectra of solid films were recorded by a Shimadzu UV–vis–NIR UV-3600 spectrophotometer.

**Work Function Measurements.** The work function values of ITO, GO, GO-SWCNT, and PEDOT:PSS films were determined by ultraviolet photoelectron spectroscopy (UPS) measurements on a Thermo Scientific ESCALAB 250Xi with a 21.2 eV He(I) source at an energy step size of 0.05 eV, base pressure of  $8 \times 10^{-10}$  mbar, and a pass energy of 2 eV. Gold foil was used to calibrate the instrument. The secondary electron cutoff (SECO) for the various layers was determined on application of a –10 V sample bias by fitting curves from five measurements of each sample.

**Density Functional Theory (DFT) Calculations.** DFT calculations were carried out using the VASP code.<sup>36</sup> The PBE exchange–correlation functional was employed in combination with projector augmented wave (PAW) type pseudo-potentials as implemented in the VASP package.<sup>37</sup> Briefly, a plane-wave kinetic energy cutoff of 450 eV and a  $k$ -grid of  $1 \times 1 \times 20$  were chosen to ensure convergence in the band structure and total energy of the (8,5) m-SWCNT. A cold (Methfessel-Paxton) smearing<sup>38</sup> of 0.2 eV was employed. Both the isolated PC<sub>71</sub>BM and (8,5) m-SWCNT structures were relaxed within DFT, and a strict tolerance of  $10^{-8}$  eV on the total energy was used to obtain an accurate ground state charge density. The interface between one unit cell of the (8,5) nanotube (172 C atoms) and PC<sub>71</sub>BM was prepared by placing the fullerene at a van der Waals distance of 0.33 nm from the sidewall of the nanotube and further relaxing the geometry. A large vacuum of >1 nm was placed in the nonrepeating directions normal to the nanotube axis to avoid spurious interactions with the image cells. The PDOS plot was obtained with a denser  $k$ -grid of  $1 \times 1 \times 40$ . No significant changes in the PDOS were observed by changing the relative orientation of the PC<sub>71</sub>BM and the nanotube.

## ■ ASSOCIATED CONTENT

### Supporting Information

Further experimental data, including work function measurements and sample characterization. This material is available free of charge via the Internet at <http://pubs.acs.org>.

## ■ AUTHOR INFORMATION

### Corresponding Authors

\*(S.R.) E-mail: [shenqiang@ku.edu](mailto:shenqiang@ku.edu).

\*(M.C.H.) E-mail: [m-hersam@northwestern.edu](mailto:m-hersam@northwestern.edu).

### Author Contributions

<sup>†</sup>These authors (M.G. and T.A.S.) contributed equally to this work. M.G. designed, fabricated, and characterized inverted geometry cells. T.A.S. prepared and characterized carbon nanotube samples and interfacial layers. Y.X. and D.J. fabricated and characterized regular geometry cells. M.B. carried out DFT calculations. K.A.L. performed work function measurements. All authors discussed results and participated in the preparation of the manuscript. J.G., S.R., T.J.M., and M.C.H. supervised the project.

### Notes

The authors declare no competing financial interest.

## ■ ACKNOWLEDGMENTS

Work at the University of Kansas (S.R.) was supported by the Army Research Office Young Investigator Program (W911NF-14-1-0443, material design/self-assembly and photovoltaics), and Department of Energy Basic Energy Sciences Award No. DE-FG02-13ER46937 (organic synthesis and coating). Work at Northwestern University (M.C.H. and T.J.M.) was supported as part of the Argonne–Northwestern Solar Energy Research (ANSER) Center, an Energy Frontier Research Center funded by the U.S. Department of Energy, Office of Science, Basic Energy Sciences under Award No. DE-SC0001059. T.A.S. and K.A.L. acknowledge graduate research fellowships through the National Science Foundation. Work at the Massachusetts Institute of Technology (M.B. and J.C.G.) was supported by an MITEI Seed Fund project. The authors thank P. Ciszek and S. Christensen at NREL for their assistance with cell certification. UPS was performed in the NUANCE facility at Northwestern University, which is supported by the NSF-MRSEC (DMR-1121262), Keck Foundation, and State of Illinois.

## ■ REFERENCES

- Ginley, D.; Green, M. A.; Collins, R. *MRS Bull.* **2008**, *33*, 355–364.
- Graetzel, M.; Janssen, R. A. J.; Mitzi, D. B.; Sargent, E. H. *Nature* **2012**, *488*, 304–312.
- Bernardi, M.; Lohrman, J.; Kumar, P. V.; Kirkeminde, A.; Ferralis, N.; Grossman, J. C.; Ren, S. *ACS Nano* **2012**, *6*, 8896–8903.
- Bindl, D. J.; Wu, M.-Y.; Prehn, F. C.; Arnold, M. S. *Nano Lett.* **2011**, *11*, 455–460.
- Jain, R. M.; Howden, R.; Tvrđy, K.; Shimizu, S.; Hilmer, A. J.; McNicholas, T. P.; Gleason, K. K.; Strano, M. S. *Adv. Mater.* **2012**, *24*, 4436–4439.
- Ramuz, M. P.; Vosgueritchian, M.; Wei, P.; Wang, C.; Gao, Y.; Wu, Y.; Chen, Y.; Bao, Z. *ACS Nano* **2012**, *6*, 10384–10395.
- Tung, V. C.; Huang, J.-H.; Kim, J.; Smith, A. J.; Chu, C.-W.; Huang, J. *Energy Environ. Sci.* **2012**, *5*, 7810–7818.
- Tyler, T. P.; Brock, R. E.; Karmel, H. J.; Marks, T. J.; Hersam, M. C. *Adv. Energy Mater.* **2011**, *1*, 785–791.
- Wang, H.; Koleilat, G. I.; Liu, P.; Jiménez-Osés, G.; Lai, Y.-C.; Vosgueritchian, M.; Fang, Y.; Park, S.; Houk, K. N.; Bao, Z. *ACS Nano* **2014**, *8*, 2609–2617.

- Avouris, P.; Freitag, M.; Perebeinos, V. *Nat. Photonics* **2008**, *2*, 341–350.
- Iijima, S. *Nature* **1991**, *354*, 56–58.
- Kroto, H. W.; Heath, J. R.; O'Brien, S. C.; Curl, R. F.; Smalley, R. E. *Nature* **1985**, *318*, 162–163.
- Saito, R.; Fujita, M.; Dresselhaus, G.; Dresselhaus, M. S. *Appl. Phys. Lett.* **1992**, *60*, 2204–2206.
- Debnath, R.; Bakr, O.; Sargent, E. H. *Energy Environ. Sci.* **2011**, *4*, 4870–4881.
- Gabor, N. M.; Zhong, Z.; Bosnick, K.; Park, J.; McEuen, P. L. *Science* **2009**, *325*, 1367–1371.
- Mayer, A. C.; Scully, S. R.; Hardin, B. E.; Rowell, M. W.; McGehee, M. D. *Mater. Today* **2007**, *10*, 28–33.
- Peters, C. H.; Sachs-Quintana, I. T.; Mateker, W. R.; Heumueller, T.; Rivnay, J.; Noriega, R.; Beiley, Z. M.; Hoke, E. T.; Salleo, A.; McGehee, M. D. *Adv. Mater.* **2012**, *24*, 663–668.
- De Volder, M. F. L.; Tawfick, S. H.; Baughman, R. H.; Hart, A. J. *Science* **2013**, *339*, 535–539.
- Green, A. A.; Hersam, M. C. *Adv. Mater.* **2011**, *23*, 2185–2190.
- Hersam, M. C. *Nat. Nanotechnol.* **2008**, *3*, 387–394.
- Tune, D. D.; Shapter, J. G. *Energy Environ. Sci.* **2013**, *6*, 2572–2577.
- Kataura, H.; Kumazawa, Y.; Maniwa, Y.; Umezū, I.; Suzuki, S.; Ohtsuka, Y.; Achiba, Y. *Synth. Met.* **1999**, *103*, 2555–2558.
- Weisman, R. B.; Bachilo, S. M. *Nano Lett.* **2003**, *3*, 1235–1238.
- Nish, A.; Hwang, J.-Y.; Doig, J.; Nicholas, R. J. *Nat. Nanotechnol.* **2007**, *2*, 640–646.
- Ye, Y.; Bindl, D. J.; Jacobberger, R. M.; Wu, M.-Y.; Roy, S. S.; Arnold, M. S. *Small* **2014**, DOI: 10.1002/smll.201400696.
- Zhang, M. L.; Wang, H.; Tian, H. K.; Geng, Y. H.; Tang, C. W. *Adv. Mater.* **2011**, *23*, 4960–4964.
- Holt, J. M.; Ferguson, A. J.; Kopidakis, N.; Larsen, B. A.; Bult, J.; Rumbles, G.; Blackburn, J. L. *Nano Lett.* **2010**, *10*, 4627–4633.
- Fuhrer, M. S.; Nygard, J.; Shih, L.; Forero, M.; Yoon, Y. G.; Mazzone, M. S. C.; Choi, H. J.; Ihm, J.; Louie, S. G.; Zettl, A.; McEuen, P. L. *Science* **2000**, *288*, 494–497.
- Rand, B. P.; Burk, D. P.; Forrest, S. R. *Phys. Rev. B* **2007**, *75*, 115327.
- Lo, M. F.; Ng, T. W.; Liu, T. Z.; Roy, V. A. L.; Lai, S. L.; Fung, M. K.; Lee, C. S.; Lee, S. T. *Appl. Phys. Lett.* **2010**, *96*, 113303.
- You, J.; Dou, L.; Yoshimura, K.; Kato, T.; Ohya, K.; Moriarty, T.; Emery, K.; Chen, C.-C.; Gao, J.; Li, G.; Yang, Y. *Nat. Commun.* **2013**, *4*, 1446.
- Betancur, R.; Romero-Gomez, P.; Martinez-Otero, A.; Elias, X.; Maymo, M.; Martorell, J. *Nat. Photonics* **2013**, *7*, 995–1000.
- Su, W. S.; Leung, T. C.; Chan, C. T. *Phys. Rev. B* **2007**, *76*, 235413.
- Buonocore, F.; Trani, F.; Ninno, D.; Di Matteo, A.; Cantele, G.; Iadonisi, G. *Nanotechnology* **2008**, *19*, 025711.
- Green, A. A.; Hersam, M. C. *Nano Lett.* **2008**, *8*, 1417–1422.
- Kresse, G.; Furthmüller, J. *Phys. Rev. B* **1996**, *54*, 11169–11186.
- Kresse, G.; Joubert, D. *Phys. Rev. B* **1999**, *59*, 1758–1775.
- Methfessel, M.; Paxton, A. T. *Phys. Rev. B* **1989**, *40*, 3616–3621.